




Article

Microstructure and Phase Composition of Novel Crossover Al-Zn-Mg-Cu-Zr-Y(Er) Alloys with Equal Zn/Mg/Cu Ratio and Cr Addition

Maria V. Glavatskikh, Ruslan Yu. Barkov , Leonid E. Gorlov, Maxim G. Khomutov 
and Andrey V. Pozdniakov 

Department of Physical Metallurgy of Non-Ferrous Metals, The National University of Science and Technology MISIS, 119049 Moscow, Russia; glavatskikh@edu.misis.ru (M.V.G.); gorlov.l@misis.ru (L.E.G.); khomutov@misis.ru (M.G.K.)

* Correspondence: barkov@misis.ru (R.Y.B.); pozdniakov@misis.ru (A.V.P.)

Abstract: The effect of 0.2%Cr addition on the structure, phase composition, and mechanical properties of the novel cast and wrought Al-2.5Zn-2.5Mg-2.5Cu-0.2Zr-Er(Y) alloys were investigated in detail. Chromium is distributed between primary crystals (5.7–6.8%) of the intermetallic phase and the aluminum solid solution (0.2%) (Al). The primary crystals contain for the main part Cr, Ti, Er(Y). The experimental phase composition is in good correlation with the thermodynamic computation data. The micron-sized solidification origin phases ($\text{Al}_8\text{Cu}_4\text{Er}$ (or Y) and Mg_2Si) and supersaturated (Al) with nano-sized $\text{Al}_3(\text{Zr,Ti})$ and E ($\text{Al}_{18}\text{Mg}_3\text{Cr}_2$) precipitates are presented in the microstructure of the novel alloys after solution treatment. The nucleation of η (MgZn_2) (0.5%), S (Al_2CuMg) (0.4%), and T (Al,Zn,Mg,Cu) (8.8%) phase precipitates at 180 °C, providing the achievement of a maximum hardness of 135 HV in the Al2.5Zn2.5Mg2.5CuYCr alloy. The corrosion potential of the novel alloy is similar to the E_{cor} of the referenced alloy, but the corrosion current density ($0.68\text{--}0.98 \mu\text{A}/\text{cm}^2$) is still significantly lower due to the formation of E ($\text{Al}_{18}\text{Mg}_3\text{Cr}_2$) precipitates and S phase precipitates of the aging origin, in addition to the T phase. The formation of E ($\text{Al}_{18}\text{Mg}_3\text{Cr}_2$) precipitates under the solution treatment provides a lower proportion of recrystallized grains (2.5–5% vs. 22.4–25.1%) and higher hardness (110 HV vs. 85–95 HV) in the Cr-rich alloys compared to the referenced alloys. Solution treated, hot and cold rolled, recrystallized, water quenched and aged at 210 °C alloys demonstrate an excellent microstructure stability and tensile properties: $YS = 299\text{--}300 \text{ MPa}$, $UTS = 406\text{--}414 \text{ MPa}$, and $El. = 9\text{--}12.3\%$.

Keywords: aluminum alloys; microstructure; mechanical properties; precipitates; erbium; yttrium



Citation: Glavatskikh, M.V.; Barkov, R.Y.; Gorlov, L.E.; Khomutov, M.G.; Pozdniakov, A.V. Microstructure and Phase Composition of Novel Crossover Al-Zn-Mg-Cu-Zr-Y(Er) Alloys with Equal Zn/Mg/Cu Ratio and Cr Addition. *Metals* **2024**, *14*, 547. <https://doi.org/10.3390/met14050547>

Academic Editors: Elena Pereloma, Jianghua Chen and Marcello Cabibbo

Received: 20 March 2024

Revised: 29 April 2024

Accepted: 4 May 2024

Published: 6 May 2024



Copyright: © 2024 by the authors. Licensee MDPI, Basel, Switzerland. This article is an open access article distributed under the terms and conditions of the Creative Commons Attribution (CC BY) license (<https://creativecommons.org/licenses/by/4.0/>).

1. Introduction

The most widely used cast and wrought aluminum alloys with medium and high strength are the alloys of the Al-Cu-(Mg) and Al-Zn-Mg-(Cu) systems [1]. The Al-Cu-(Mg) alloys demonstrate a good strength at room and elevated temperatures but exhibit low casting properties and corrosion resistance [1–4]. The high strength wrought Al-Zn-Mg-(Cu) alloys lack low casting and corrosion properties, and low heat resistance [1–3,5,6]. General principles of eutectic forming elements alloying were employed to enhance the castability and heat resistance of both groups of alloys [4,5,7,8]. A novel approach to developing crossover alloys based on using aluminum alloy scraps was presented [9]. The crossover alloys combine the properties of mixed alloys of different series [10–17]. A novel crossover Al-5.64Mg-5.43Zn-0.51Cu alloy with ultra-high strength was developed based on Al-Mg/Al-Zn-Mg-(Cu) systems [13]. A significantly earlier method of improving of casting properties and heat and corrosion resistance of the Al-Zn-Mg-(Cu) alloys was suggested [18–21]. This method was based on obtaining alloys with a Zn/Mg ratio near [18–21]. Novel cast and wrought Al-3Zn-3Mg-3Cu-Zr-Y(Er) alloys with improved heat resistance

were developed based on the principles of the Zn/Mg ratio [21]. On the other hand, this alloy could be classified as a crossover alloy, based on the Al-Cu/Al-Zn-Mg-(Cu) systems, with additional alloying by rare earth metals. As a result, the novel Al-3Zn-3Mg-3Cu-Zr-Y(Er) alloy combines the improved casting properties of the cast Al-Zn-Mg alloys [1,3,5,6], good strength of the Al-Zn-Mg-Cu alloys [1], and improved heat resistance of the Al-Cu alloy [1,2,4]. Zn, Mg, and Cu in the ratio used provide aging strengthening due to nucleation of the T' precipitates [13,16,21]. The presence of Cu and Er in the alloy leads to formation of a fine Al₈Cu₄Er phase during solidification, which improves casting properties and heat resistance [22,23]. Zr and Er(Y) provide precipitate strengthening due to nucleation of the L1₂-Al₃(Zr,Er(Y)) precipitates during the solution treatment [21,23–30]. The most important effect of Er(Y) is in increasing the solidus temperature of the alloy. A higher solidus temperature is important to obtain improved heat resistance and for increasing the hot deformation temperature [21]. Consequently, the novel Al-3Zn-3Mg-3Cu-Zr-Y(Er) alloy shows good strength at room and elevated temperatures after quenching and aging of the ingots and rolled sheets [21].

The addition of trace chromium, along with other rare earth and transition metals, to the Al-Zn-Mg-Cu alloys can lead to the refinement of the grain structure, significantly and improve strength, recrystallization, corrosion, and fracture behavior, due firstly to the formation of Al₇Cr (Al₄₅Cr₇) or E (Al₁₈Mg₃Cr₂) precipitates [1,2,31–43]. AlCrSi or α -Al(Mn,Cr,Fe)Si precipitates may nucleate in the Si containing aluminum alloys [44,45]. Chromium may substitute aluminum atoms in the L1₂-structured precipitates of the (Al,Cr)₃(Zr,Yb) phase, which improves the coarsening-resistance of the Al₃Zr and Al₃(Zr,Yb) phases at 500 °C [46].

The aim of the present study is to determine the effect of 0.2% Cr addition on the microstructure, mechanical and corrosion behavior of the Al-2.5Zn-2.5Mg-2.5Cu-Er(Y)-Zr-Ti-Fe-Si alloy in the as-cast, quenched and aged, rolled and annealed states. The content of the primary alloying elements was decreased to make the alloys more technologically useful under thermo-mechanical treatment and to improve plasticity.

2. Materials and Methods

2.1. Alloys Preparation

The referenced Al₃Zn₃Mg₃CuEr(Y) [22] and novel Al_{2.5}Zn_{2.5}Mg_{2.5}CuEr(Y)Cr alloys were melted using pure Al (99.7%), Zn (99.7%), Mg (99.5%), Cu (99.5%) and Al-10Er, Al-10Y, Al-5Zr, Al-10Cr and Al-5Ti-1B master alloys in a resistance furnace in air. The content of the Zn, Mg, Cu, Y, and Er in the alloys after melting was measured by an electron diffraction X-ray (EDX) detector X-max 80 in a scanning electron microscope (SEM) TESCAN VEGA 3LMH (Tescan, Brno, Kohoutovice, Czech Republic) (Table 1). The melting process and pouring of the melt was at a temperature of 800–810 °C. Pure Cu and master alloys were introduced into the melt of Al separately, step by step. Then, pure Mg was introduced using Ti bell, and finally Zn was introduced before pouring into a copper water-cooling (CM) and steel molds (SM). The CM mold had internal sizes of 120 × 40 × 20 mm³, and the ingot's weight was about 300 g. The ingots obtained in the CM were used for rolling. The cylinder bars obtained in the SM had a diameter of 24 mm and length of 290 mm with a weight of about 800 g. The SM bars were used for tensile test sample preparation. The hot tearing sensitivity was measured using “pencil probe”, and the hot cracking index (HCI) was determined [2–5].

Table 1. Chemical composition of the investigated and referenced alloys in wt.%. (SEM EDX).

Alloy	Al	Zn	Mg	Cu	Zr	Ti	Fe and Si	Y or Er	Cr
Al ₃ Zn ₃ Mg ₃ CuY	bal.	3.1	2.9	2.9	0.2	0.1	0.3	0.6	-
Al _{2.5} Zn _{2.5} Mg _{2.5} CuYCr	bal.	2.6	2.6	2.7	0.2	0.1	0.3	0.5	0.2
Al ₃ Zn ₃ Mg ₃ CuEr	bal.	2.9	2.8	3.0	0.2	0.1	0.3	1.4	-
Al _{2.5} Zn _{2.5} Mg _{2.5} CuErCr	bal.	2.6	2.5	2.6	0.2	0.1	0.3	1.3	0.2

2.2. Microstructure and Phase Composition Analyses

Thermodynamic computations (TC) of the multicomponent phase diagram, phase equilibria and non-equilibrium solidification of the alloy were carried out in the Thermo-Calc software (TCW5, Thermo-Calc Software AB, Stockholm, Sweden) in the TTAL5 database.

The optical Zeiss microscope (OM) and electron backscattered diffraction (EBSD) HKL detector (NordlysMax) in SEM were used to analyze the ingots' and rolled sheets' grain structure. The polarized light in the OM was applied to grain structure visualization. Microstructure and phase identification were investigated in detail in SEM. SEM images were obtained with a back-scattered electron (BSE) detector at $\times 3000$ magnification and voltage of 20 kV. SEM phase identification was performed using the electron diffraction X-ray (EDX) detector X-max 80. The EBSD maps were processed in an area of $250 \times 250 \mu\text{m}^2$ with a $0.5 \mu\text{m}$ step size to identify high angle grain boundaries (HAGBs with misorientation $>15^\circ$) and low angle grain boundaries (LAGBs with misorientation $<15^\circ$).

2.3. Preparation of the Specimens for Microstructure Investigation

Samples for optical microscopy (OM) and scanning electron microscopy (SEM) analysis underwent mechanical grinding and polishing. Struers Labopol equipment was utilized for these processes, employing grinding disk sheets with grit sizes of #800, #1200, #2000, and #4000, along with OP-S suspension for specimen preparation. For OM, the grain structure was electrochemically etched using Barker's reagent (46 mL of HBF_4 , 7 g of HBO_3 , and 970 mL of H_2O) at 15–25 V and 0–5 °C. The average grain size was determined using the random secant method based on three images.

2.4. Heat Treatment and Rolling Processing

The Labsys Setaram differential scanning calorimeter (DSC) from SETARAM Instrumentation (Caluire, France) was used to determine the solidus and phase transformation temperatures of the alloys. Solution treatment, carried out at 480–520 °C for 3 and 6 h, occurred in a resistant furnace with an accuracy of approximately 1 °C. Subsequent aging after solution treatment and water quenching took place at 120–210 °C in the same furnace with an accuracy of about 3 °C. Following solution treatment at 480–520 °C and water quenching, the ingot underwent hot rolling at 500 °C, starting from a thickness of 20 mm to 5 mm and, at room temperature, to 1 mm thickness sheets. Samples from the rolled sheets underwent annealing at temperatures ranging from 150–500 °C for different durations to investigate grain structure, hardness, and tensile properties. The heat treatment was processed in the air atmosphere. The rolled sheets were subsequently recrystallized at 520 °C for 15 min, water-quenched, and aged at 120–210 °C to determine their tensile properties.

2.5. Mechanical Properties' Measurements and Calculations

Hardness measurements were conducted using the Vickers method under a 5 kg load. Tensile samples were stretched using a Zwick/Roell Z250 Allround test machine (Zwick/Roell, Kennesaw, GA, USA) with an extensometer. The samples, featuring a gage diameter of 6 mm and gauge length of 42 mm, were cut from heat-treated ingots obtained in a steel mold. Additionally, tensile samples with a gauge width of 6 mm and gauge length of 22 mm were cut from 1 mm thickness sheets. A minimum of 3 samples were tested per state, and the average value was calculated.

2.6. Electro-Chemical Corrosion Tests

Samples with diameter of 10 mm and length of 60 mm were used for electrochemical corrosion tests with potentiostat-galvanostat P-45X (Electro Chemical Instruments, Chernogolovka, Russia). Tests were performed in the 3.5%NaCl water solution. AgCl_2 electrode was used as reference electrode and graphite electrode as counter electrode.

3. Results and Discussion

3.1. Thermodynamic Calculation of the Phase Composition

The calculated equilibrium polythermal section in the Al-2.5Zn-2.5Mg-2.5Cu-0.2Zr-0.1Ti-0.15Si-0.15Fe-(0–0.4)Cr system (a) and non-equilibrium solidification curve (b) of the Al2.5Zn2.5Mg2.5CuCr alloy are presented in Figure 1. Increasing the Cr concentration to 0.4% in the Al-2.5Zn-2.5Mg-2.5Cu-0.2Zr-0.1Ti-0.15Si-0.15Fe alloy did not affect the liquidus temperature and type of primary crystals (Figure 1a). The equilibrium solidification of the Al2.5Zn2.5Mg2.5CuCr alloy starts from the $\text{Al}_3(\text{Zr,Ti})$ phase formation (Figure 1). The first Cr content Al_7Cr phase solidified after primary $\text{Al}_3(\text{Zr,Ti})$ at a chromium concentration of more than 0.12%. The non-equilibrium solidification curve calculated by the Scheil model works on the assumption that the distributive and equalizing diffusion in a liquid phase is completely processed. However, the formation of the primary intermetallic phases, such as $\text{Al}_3(\text{Zr,Ti})$ and Al_7Cr , may be suppressed. The as-cast microstructure should consist of the Al_3Fe , Mg_2Si , $\text{Al}_7\text{Cu}_2\text{Fe}$, $\text{S}(\text{Al}_2\text{CuMg})$, and MgZn_2 phases in accordance with the non-equilibrium solidification curve (Figure 1b). The described theoretical specifics may be applied to the Er(Y)-free alloy. The microstructure of the investigated alloys will be analyzed in detail in the next part.

Liquidus temperature (T_L), equilibrium solidus temperature (T_S), temperature of the 65% of solid phases formation ($T_{65\%}$) and non-equilibrium solidus temperature (T_{NS}) were determined from Figure 1b (Table 2). The effective solidification range (ESR) and the HCI of the alloys may be calculated using the non-equilibrium solidification curve [5]. The ESR of the Al-Zn-Mg-Cu alloys is in a range between $T_{65\%}$ and T_{NS} [5]. The ESR of the Al2.5Zn2.5Mg2.5CuCr is equal to 131 °C, and the calculated HCI is equal to 14 mm. HCI = 14 is the index of the low sensitivity of the alloy to crack formation of solidification origin [5].

Table 2. Critical temperatures (TC), ESR, and HCI of the Al2.5Zn2.5Mg2.5CuCr alloy.

T_L , °C	T_S , °C	$T_{65\%}$, °C	T_{NS} , °C	ESR, °C	HCI _c , mm
756	521	606	475	131	14

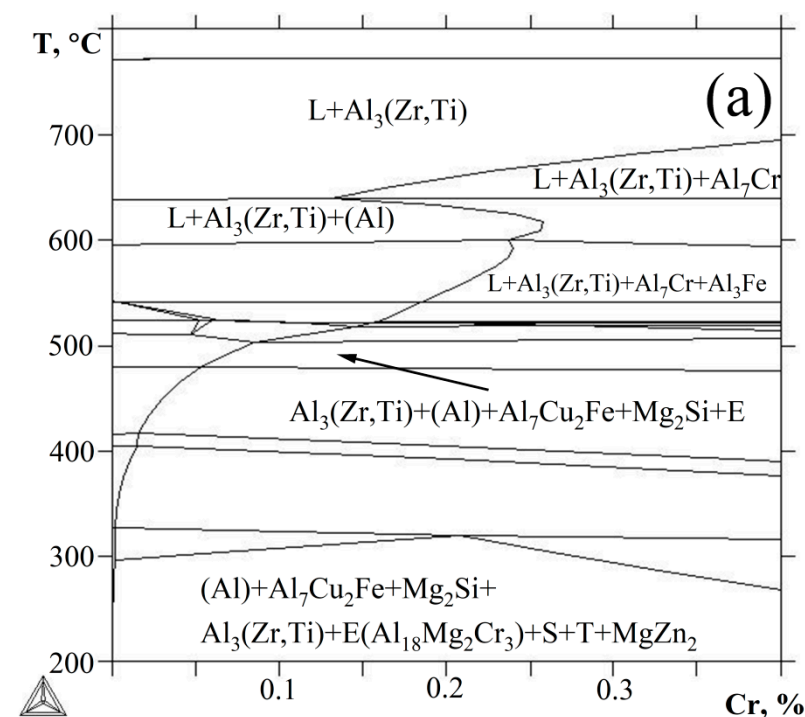


Figure 1. Cont.

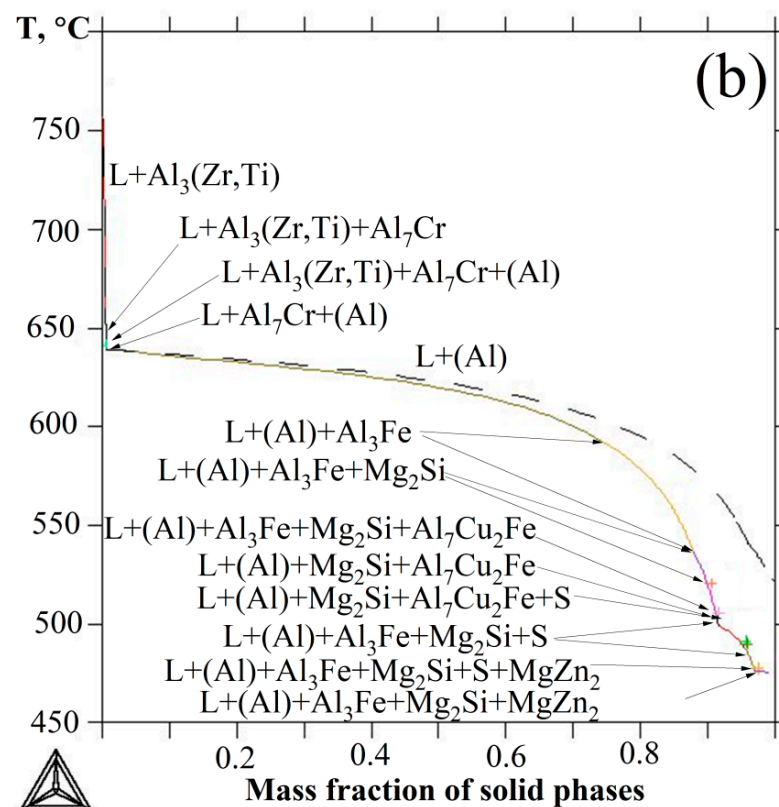


Figure 1. (a) Polythermal section Al-2.5Zn-2.5Mg-2.5Cu-0.1Ti-0.15Si-0.15Fe-0.2Zr-(0–0.4)Cr and (b) non-equilibrium solidification curve of the Al2.5Zn2.5Mg2.5CuCr alloy (dash line—equilibrium cooling curve) (TC).

3.2. As-Cast Microstructure and Phase Composition

The alloy casting was performed in SM and CM. The cooling rate during solidification in the CM is higher than in the SM. Figure 2 illustrates the distinctions in the grain and dendritic cell structure of the as-cast alloys. The different cooling rate have no significant effect on the grain structure of the Cr-free Al3Zn3Mg3CuEr(Y) alloys, as demonstrated in [21]. A finer grain structure with a size of $45 \pm 10 \mu\text{m}$ was indicated in the Al3Zn3Mg3CuEr alloy in comparison with the Al3Zn3Mg3CuY alloy ($80 \pm 10 \mu\text{m}$) [21]. Chromium alloying of the Al2.5Zn2.5Mg2.5CuEr(Y) alloys makes the grain structure the same (Figure 2). However, the cooling rate has a limited impact on the grain size of the Al2.5Zn2.5Mg2.5CuEr(Y) alloys (Figure 2). The average grain size in the CM is $50 \pm 10 \mu\text{m}$ and in the SM $90 \pm 15 \mu\text{m}$ (Figure 2). The significant effect of 0.2Cr, 0.2Mn, 0.14Zr, and 0.03Ti on the grain structure of the Al-Zn-Mg-Cu cast alloy was demonstrated earlier [43]. The impact of chromium and manganese is linked to reducing the surface tension between liquid aluminum and solid $\text{Al}_3(\text{Ti}_x\text{Zr}_{1-x})$ (Al_3Ti , Al_3Zr) particles [43]. Our previous investigations of the Cr effect on the structure and properties of Al-Cu-Y(Er)-Zr-(Mg) alloys show the same significant effect of grain refining [47,48]. The additional refining effect was explained by the nucleation of primary $\text{Al}_{75-80}\text{Cu}_{10-12}\text{Er}(\text{Ti})_{3-4}\text{Cr}_7$ phase particles, which could serve as nucleation centers of the primary aluminum solid solution [47,48]. The lower cooling rate during solidification in the CM provides a finer dendritic cell structure (SDAS) (Figure 2). However, as demonstrated in [21,49] such differences in the SDAS size do not have a significant impact on mechanical properties.

The microstructure (SEM) of the as-cast samples of the Al2.5Zn2.5Mg2.5CuYCr and Al2.5Zn2.5Mg2.5CuErCr alloys is presented in Figure 3. The detailed investigation of the as-cast microstructure of the referenced Al3Zn3Mg3CuEr(Y) alloys was carried out in [21]. Solidification of the primary Cr-rich crystals is the main difference in the microstructure between investigated and referenced alloys ([21] and Figure 3). Chromium is distributed

between primary crystals (5.7–6.8%) and the aluminum solid solution (0.2%) (Figure 3 and Table 1). The primary crystals contain for the main part Cr, Ti, Er(Y), with additional dissolving of Zn, Mg, Cu (Figure 3 and Table 3). The different ternary intermetallic phases may solidify in accordance with the ternary phase diagram of the Al–Er–Cr [50], Al–Cu–Cr [51], Al–Er–Mg [52], Al–Cr–Mg [53] and Al–Ti–Er [54] systems. Information on more complex phases was not found in the literature. In this case, it is very difficult to identify the primary crystals' formula. The main alloying elements Zn/Mg/Cu provide the formation of the T (Al,Zn,Mg,Cu) phase (distribution of alloying elements into the red rectangle). The main Zn/Mg/Cu containing phases in the Er(Y)-free alloys should be S (Al_2CuMg) and η (MgZn_2), in accordance with TC (Figure 1). These phases may be presented in the microstructure, but their identification through SEM is difficult due to the very low volume fraction. Copper and erbium (or yttrium) lead to solidified $\text{Al}_8\text{Cu}_4\text{Er}$ (or Y) phase particles with dissolved Zn, Fe, and Mg (Figure 3 and Table 3). Er-rich particles of the Al_3Er phase were also identified (Figure 3b). The presence of silicon impurity leads to formation of the Mg_2Si phase (Figure 3). EDX measurements indicate Zr and Y or Er concentrations in the (Al) as 0.3% and 0.2% or 0.3%, respectively (Table 3).

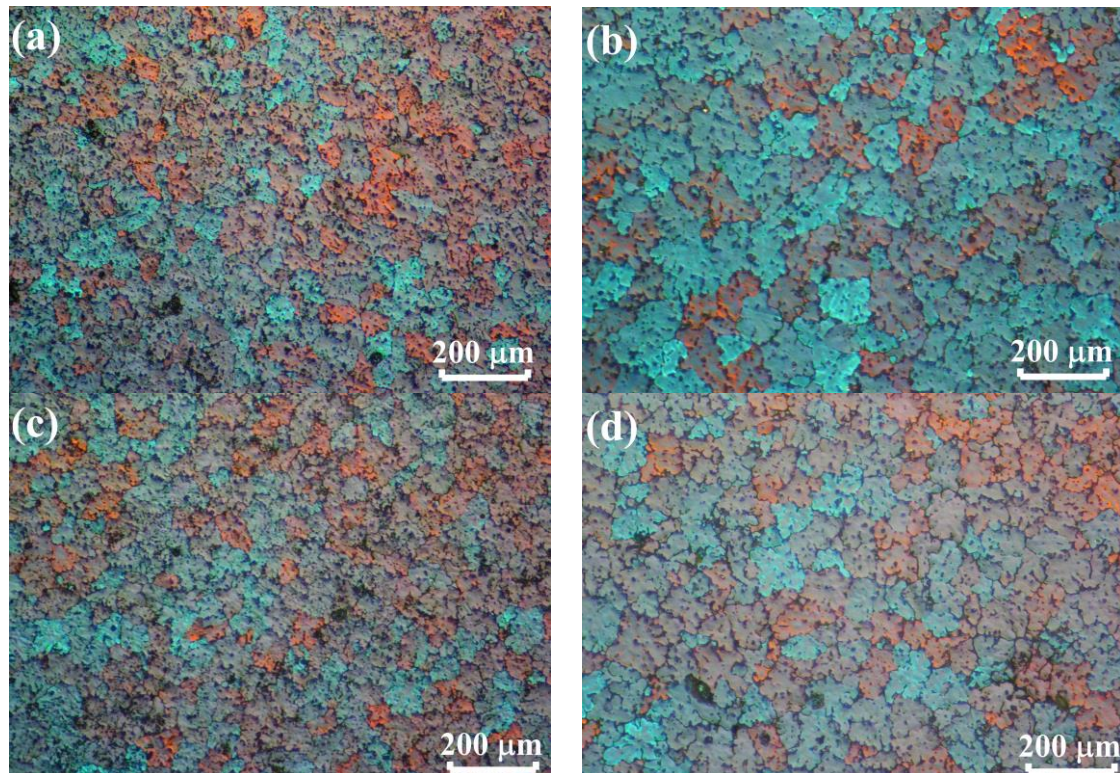


Figure 2. As-cast grain structure (polarized light in OM) of the (a,b) $\text{Al}_{2.5}\text{Zn}_{2.5}\text{Mg}_{2.5}\text{CuYCr}$ and (c,d) $\text{Al}_{2.5}\text{Zn}_{2.5}\text{Mg}_{2.5}\text{CuErCr}$ alloys poured into (a,c) CM and (b,d) SM.

Table 3. Composition of the phases in the as-cast state in wt.% (EDX SEM).

Phase	Al	Zn	Mg	Cu	Ti	Fe	Y or Er	Cr
1 (Figure 3a)	bal.	4.5	2.7	27	-	1.9	11.2	-
2 (Figure 3a)	bal.	3.7	2.8	3.7	5.8	-	11.6	6.8
(Al) (Figure 3a)	bal.	2.1	1.9	1.0	-	0.3Zr	0.2	0.2
1 (Figure 3b)	bal.	2.8	1.6	26.5	-	1.6	11.2	-
2 (Figure 3b)	bal.	3.4	2.5	3.4	4.7	-	16.2	5.7
(Al) (Figure 3b)	bal.	1.8	1.5	0.9	-	0.3Zr	0.3	0.2

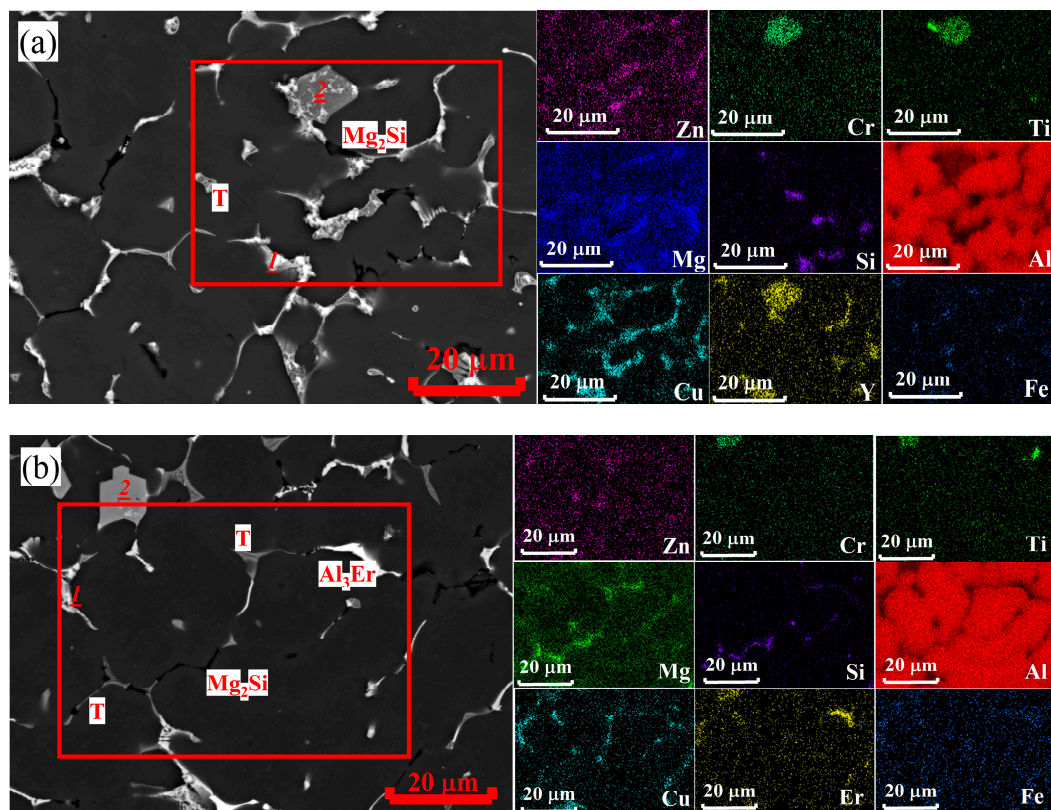


Figure 3. As-cast microstructure of the (a) Al_{2.5}Zn_{2.5}Mg_{2.5}CuYCr and (b) Al_{2.5}Zn_{2.5}Mg_{2.5}CuErCr alloys (distribution of alloying elements into red rectangle and EDX spectra from phase particles).

3.3. Evaluation of the Microstructure under Solution Treatment

The DSC-heating curves of the Al_{2.5}Zn_{2.5}Mg_{2.5}CuYCr and Al_{2.5}Zn_{2.5}Mg_{2.5}CuErCr alloys are shown in Figure 4. The melting behavior of both alloys is similar. Distinct peaks are observed in the heat flow vs. temperature dependencies. Melting of the T, Al₇Cu₂Fe, and Mg₂Si phases in the reactions at temperatures of 492–493 °C, 524–530 °C, and 550 °C were found in the DSC-heating curves. These results are in good agreement with the TC (Figure 1b) and melting behavior of the referenced Al₃Zn₃Mg₃CuEr(Y) alloys [21]. The fourth peak corresponds to the melting of the Al₈Cu₄Er(or Y) phase particles and the fifth to the (Al) melting. The two-stage mode of the solution treatment was used: 480 °C for 3 h and 520 °C for 6 h. The same mode was used in the referenced alloys [21]. The non-equilibrium Zn/Mg/Cu containing phases dissolved at the first stage. The equilibrium phases fragmentized and spheroidized more completely at the second stage.

As-solution treated microstructures of the Al_{2.5}Zn_{2.5}Mg_{2.5}CuYCr and Al_{2.5}Zn_{2.5}Mg_{2.5}CuErCr alloys are demonstrated in Figure 5. The T phase completely dissolved, and the equilibrium phases fragmentized and spheroidized. The results of the microstructure investigation after the solution treatment at 520 °C correlate with TC (Table 4). The Mg₂Si and Al₃Fe phases of the solidification origin and Al₃(Zr,Ti) and E (Al₁₈Mg₃Cr₂) precipitates should be in equilibrium with the aluminum solid solution in the Er(Y) free alloy (Table 4). The Al₃(Zr,Ti) and E (Al₁₈Mg₃Cr₂) phase precipitates must be nucleated from the supersaturated aluminum solid solution under solution treatment. The Zn/Mg/Cu concentrations in the (Al) increased due to the dissolving of the T phase of the solidification origin (Figure 5 and Table 5). The main effect of the Er(Y) on the composition of (Al) is in the decrease in the Cu content due to the Al₈Cu₄Er(or Y) phase formation after cast. As a result, the nominal Cu content in the (Al) is 1.4–1.6% (Table 5) in comparison with the TC data (2.5% Cu in (Al) (Table 4)). However, the Cu concentration in the (Al) in the Al_{2.5}Zn_{2.5}Mg_{2.5}CuYCr and Al_{2.5}Zn_{2.5}Mg_{2.5}CuErCr alloys is higher than in the referenced alloy by 0.2–0.3% (Table 5).

The Er(Y) content in the alloy determines the fraction of the $\text{Al}_8\text{Cu}_4\text{Er(or Y)}$ phase. The lower Cu is needed for formation of the $\text{Al}_8\text{Cu}_4\text{Er(or Y)}$ phase at a lower content of Er(Y) in the alloy. As a result, a higher Cu concentration in the (Al) and lower volume fraction of $\text{Al}_8\text{Cu}_4\text{Er(or Y)}$ phase is seen in the investigated alloys than in the referenced alloys. The micron sized solidification origin phases ($\text{Al}_8\text{Cu}_4\text{Er(or Y)}$ and Mg_2Si) and supersaturated (Al) with nanosized $\text{Al}_3(\text{Zr,Ti})$ and E ($\text{Al}_{18}\text{Mg}_3\text{Cr}_2$) precipitates are presented in the microstructure of the novel $\text{Al}_{2.5}\text{Zn}_{2.5}\text{Mg}_{2.5}\text{CuYCr}$ and $\text{Al}_{2.5}\text{Zn}_{2.5}\text{Mg}_{2.5}\text{CuErCr}$ alloys (Figure 5 and Tables 4 and 5). The detailed evaluation of $\text{Al}_3(\text{Zr,Ti})$ and E ($\text{Al}_{18}\text{Mg}_3\text{Cr}_2$) precipitates will be investigated in future work.

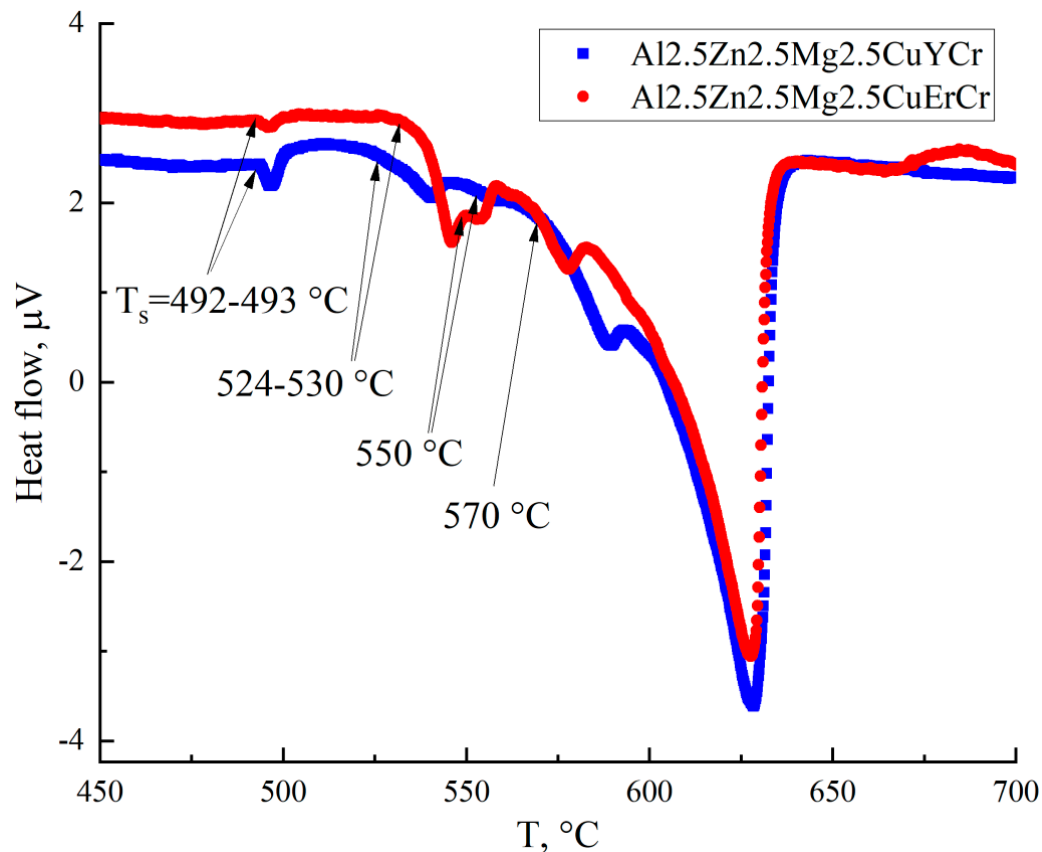


Figure 4. Heat flow vs. temperature during heating of the as-cast alloys (DSC-heating curves).

Table 4. Mass fraction of phases and concentration of alloying elements in the (Al) at 520 °C (TC).

(Al)	Al_3Fe	E ($\text{Al}_{18}\text{Mg}_3\text{Cr}_2$)	Mg_2Si	$\text{Al}_3(\text{Zr,Ti})$
bal. (2.5Zn-2.4Mg-2.5Cu-0.1Cr)	0.4	0.3	0.25	0.35

Table 5. Concentration of the Zn/Mg/Cu in (Al) in mass.% (EDX SEM).

Alloy	As-Cast State			480 °C, 3 h + 520 °C, 6 h		
	Zn	Mg	Cu	Zn	Mg	Cu
$\text{Al}_{2.5}\text{Zn}_{2.5}\text{Mg}_{2.5}\text{CuYCr}$	2.1	1.9	1.0	2.9	2.9	1.6
$\text{Al}_3\text{Zn}_3\text{Mg}_3\text{CuY}$ [22]	2.2	2.2	1.0	3.1	3.1	1.3
$\text{Al}_{2.5}\text{Zn}_{2.5}\text{Mg}_{2.5}\text{CuErCr}$	1.8	1.5	0.9	2.8	2.8	1.4
$\text{Al}_3\text{Zn}_3\text{Mg}_3\text{CuEr}$ [22]	2.2	1.9	1.0	3.0	3.0	1.2

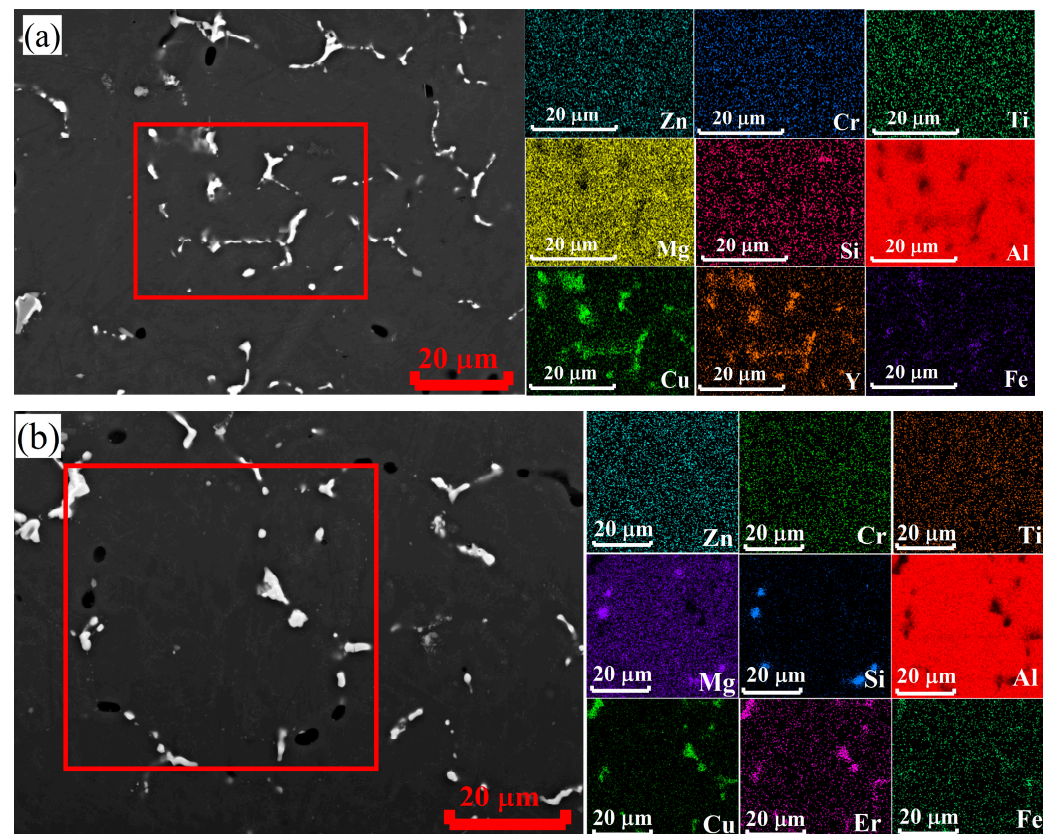


Figure 5. As-solution treated microstructure of the (a) Al_{2.5}Zn_{2.5}Mg_{2.5}CuYCr and (b) Al_{2.5}Zn_{2.5}Mg_{2.5}CuErCr alloys (distribution of alloying elements into red rectangle and EDX spectra from phases).

3.4. Aging Behavior and Mechanical Properties of Cast Alloy

Metastable modifications of the η , S, and T phases are expected to nucleate in the (Al) during aging at 120–210 °C after solution treatment and quenching of the Al_{2.5}Zn_{2.5}Mg_{2.5}CuYCr and Al_{2.5}Zn_{2.5}Mg_{2.5}CuErCr alloys in accordance with the TC (Table 6). The η and T phase precipitates are anticipated to contribute hardening at lower aging temperatures (Table 4). S phase precipitates substitute η phase with increasing aging temperature to 210 °C (Table 6). The aging hardening of the referenced Al₃Zn₃Mg₃CuEr(Y) alloys were connected with formation of T phase precipitates only ([21] and Table 6).

Table 6. Mass fraction of phases in equilibrium with the (Al) at 120–210 °C (TC).

Alloy	Composition of (Al)			Phase Composition at 120–210 °C		
	Zn	Mg	Cu	η	S	T
Al _{2.5} Zn _{2.5} Mg _{2.5} CuYCr	2.9	2.9	1.6	1.4–0	0–0.8	8.9–8.4
Al _{2.5} Zn _{2.5} Mg _{2.5} CuErCr	2.8	2.8	1.4	0.7–0	0–0.3	9.1–8.3
Al ₃ Zn ₃ Mg ₃ CuEr(Y) [22]	3.0	3.0	1.2	-	-	9.9–8.7

The HV curves at different aging temperatures for the Al_{2.5}Zn_{2.5}Mg_{2.5}CuYCr and Al_{2.5}Zn_{2.5}Mg_{2.5}CuErCr alloys are compared with the referenced Al₃Zn₃Mg₃CuEr(Y) alloys in Figure 6. The as-quenched hardness of the investigated alloys is nearly the same at 72–77 HV (Figure 6). The aging of the alloys at 120–150 °C is processed with similar hardening (Figure 6a,b). However, an increase in the aging temperature to 180–210 °C provides a higher level of hardening in the investigated alloys compared to the referenced alloys (Figure 6b,c). The nucleation of η (0.5%), S (0.4%), and T (8.8%) precipitates at 180 °C achieves the maximum hardness of 135 HV in the Al_{2.5}Zn_{2.5}Mg_{2.5}CuYCr alloy (Figure 6c).

However, as must be noted, the same hardening effect was achieved after aging at 210 °C (Figure 6d). The heat resistant alloys must be aged at a temperature higher or the same as the operating temperature. The investigated alloys were aged at 210 °C for 3 h before tensile tests at temperatures of 20 °C and 200 °C.

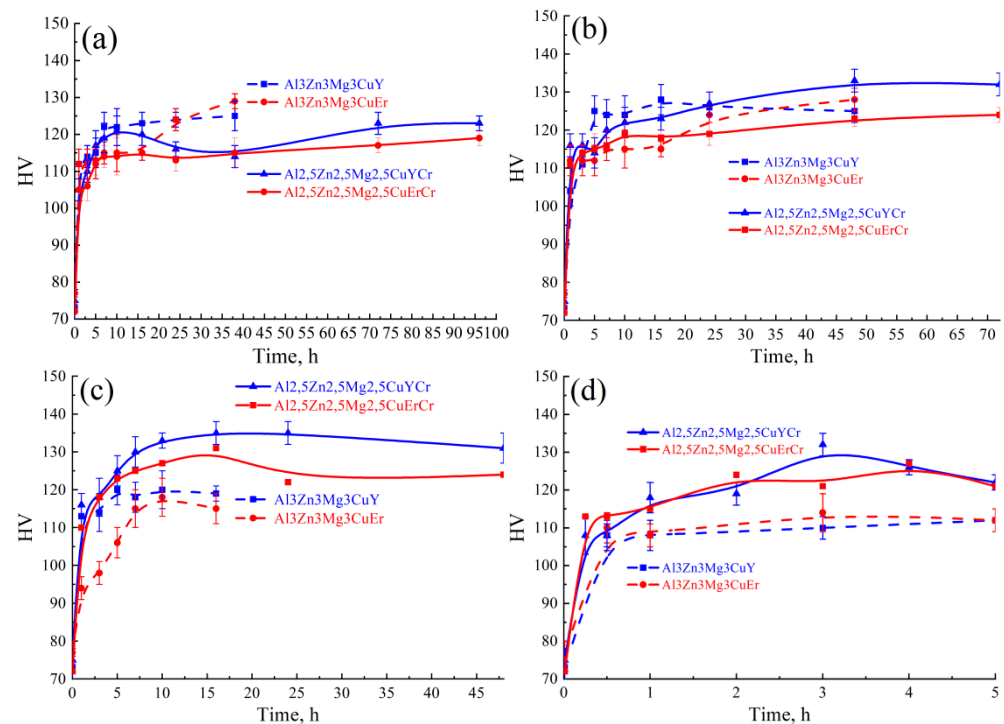


Figure 6. HV curves of cast alloys at different aging temperatures of (a) 120 °C, (b) 150 °C, (c) 180 °C, and (d) 210 °C after solution treatment and quenching.

The average values of yield strength (YS), ultimate tensile strength (UTS), and elongation (El.) at temperatures of 20 °C and 200 °C are summarized in Table 7. The novel alloys incorporate 0.2% Cr, while Zn/Mg/Cu content is reduced by 1.5%. While the tensile properties of the novel alloys are slightly lower than those of the referenced alloys, they remain significantly higher than those of the commercial cast 771.0 (7Zn-0.9Mg-0.13Cr) alloy, which exhibits YS = 185 MPa after aging at 205 °C for 6 h [1].

Table 7. YS, UTS, and El. of alloys aged at 210 °C for 3 h at temperatures of 20 °C and 200 °C.

Alloy	YS, MPa	UTS, MPa	El., %
20 °C			
Al2.5Zn2.5Mg2.5CuYCr	257 ± 4	298 ± 1	1.4 ± 0.1
Al2.5Zn2.5Mg2.5CuErCr	260 ± 1	310 ± 5	2 ± 0.3
Al3Zn3Mg3CuEr(Y)	270–280	330–340	2–3
200 °C			
Al2.5Zn2.5Mg2.5CuYCr	233 ± 5	245 ± 4	7 ± 0.6
Al2.5Zn2.5Mg2.5CuErCr	215 ± 3	228 ± 5	5 ± 0.5
Al3Zn3Mg3CuEr(Y)	225–230	237–250	3.5–5.2

3.5. Electrochemical Corrosion Behavior

A lower corrosion current density (I_{cor}) value and higher corrosion potential (E_{cor}) are indicative of better corrosion resistance of the alloy, as per Faraday's law. The polarization curves of the investigated and referenced Er(Y)-free and Cr-free alloys are presented in Figure 7. The Tafel approximation was used to determine the I_{cor} values. The Er(Y)-free and Cr-free Al3Zn3Mg3Cu alloys exhibit the highest I_{cor} value of 4.81 $\mu\text{A}/\text{cm}^2$. The

Er(Y) alloying provides a significant increase in the corrosion resistance. The I_{cor} values decreased to 0.23–1 $\mu\text{A}/\text{cm}^2$ and E_{cor} increased from 0.689 V to 0.705–0.71 V (Table 8). The increase in corrosion resistance may be attributed to the formation of the T phase precipitates in the $\text{Al}_3\text{Zn}_3\text{Mg}_3\text{CuEr(Y)}$ alloys versus η , S, and T phase precipitates in the $\text{Al}_3\text{Zn}_3\text{Mg}_3\text{Cu}$ alloy (based on TC in [21]). The second reason is the increase in the $\text{Al}_3(\text{Zr,Er(or Y)})$ precipitates' density in the $\text{Al}_3\text{Zn}_3\text{Mg}_3\text{CuEr(Y)}$ alloys in comparison with Al_3Zr in the $\text{Al}_3\text{Zn}_3\text{Mg}_3\text{Cu}$ alloy [21]. The corrosion resistance of the investigated $\text{Al}_{2.5}\text{Zn}_{2.5}\text{Mg}_{2.5}\text{CuYCr}$ and $\text{Al}_{2.5}\text{Zn}_{2.5}\text{Mg}_{2.5}\text{CuErCr}$ alloys is the same as for the Cr-free alloys with higher Zn/Mg/Cu content. The main difference of the Cr-rich alloys is the formation of E ($\text{Al}_{18}\text{Mg}_3\text{Cr}_2$) precipitates and S phase precipitates of aging origin, in addition to the T phase (Tables 4 and 6). As a result, the corrosion potential of the novel alloy is similar to the E_{cor} of $\text{Al}_3\text{Zn}_3\text{Mg}_3\text{Cu}$ referenced alloy, but the corrosion current density is still significantly lower (Table 8). The positive effect of the rare earth and transition metals on the corrosion resistance of the Al–Zn–Mg–Cu alloys was described earlier [31,33,35,36,41].

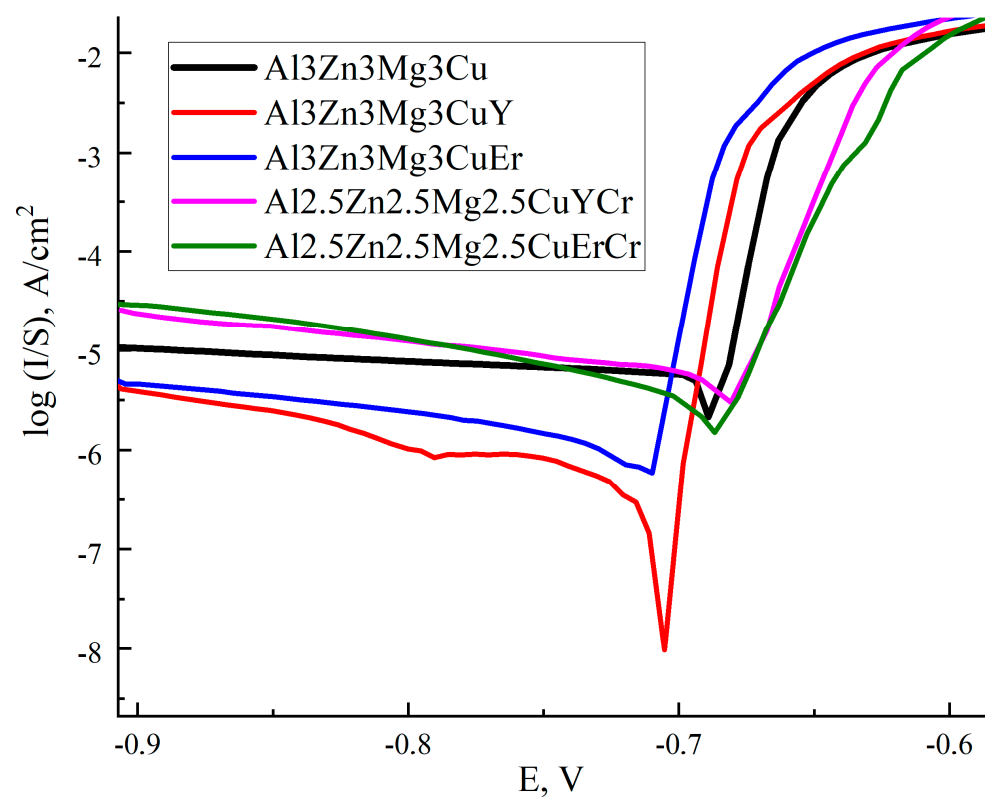


Figure 7. Polarization curves of the investigated and referenced alloys after casting, solution treatment, quenching and aging at 210 °C.

Table 8. Electrochemical corrosion parameters of the alloys.

Alloy	E_{cor} , V	I_{cor} , $\mu\text{A}/\text{cm}^2$
$\text{Al}_3\text{Zn}_3\text{Mg}_3\text{Cu}$	−0.689	4.81
$\text{Al}_3\text{Zn}_3\text{Mg}_3\text{CuY}$	−0.705	0.23
$\text{Al}_3\text{Zn}_3\text{Mg}_3\text{CuEr}$	−0.710	1.00
$\text{Al}_{2.5}\text{Zn}_{2.5}\text{Mg}_{2.5}\text{CuYCr}$	−0.681	0.98
$\text{Al}_{2.5}\text{Zn}_{2.5}\text{Mg}_{2.5}\text{CuErCr}$	−0.687	0.68

3.6. Recovery and Recrystallization Behavior of Rolled Sheets

The recovery and recrystallization processes are accelerated by annealing the cold deformed material. The nano-sized precipitates effectively pinned the dislocation motion and migration of the sub-grains and grain boundaries [28,36,41]. On the other hand, micron-sized intermetallic particles serve as effective centers for nucleation of recrystallized grains, relying on the particle stimulated nucleation effect [41,55–60]. These processes take place in the investigated alloys. The Cr addition provides for the increase in the deformation strengthening and achieving higher hardness in the as-rolled state (Figure 8). Consequently, the rate of the hardness decrease in the Cr-rich alloys with lower Zn/Mg/Cu content is higher during annealing up to 200 °C. The main processes in this stage are the decreasing of the point and linear defects density. The effect of the Cr containing precipitates becomes visible from 200 °C when the rate of the hardness reduction decreases (Figure 8).

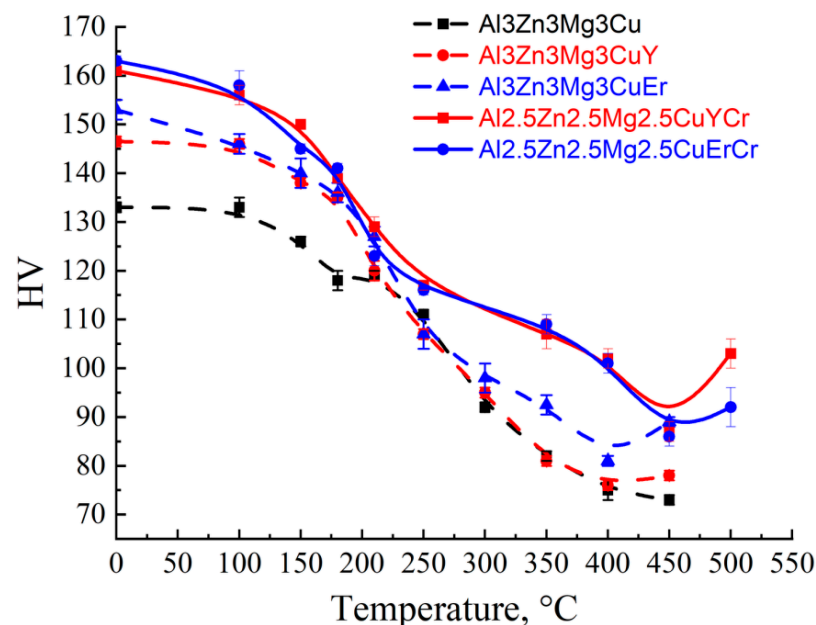


Figure 8. HV vs. temperature dependencies of the alloys rolled sheets after 1 h of annealing.

The second stage of recovery is the formation of the sub-grain structure with LAGBs. The first recrystallized grains were observed after 1 h of annealing at 350 °C (Figure 9). The fraction of recrystallized grains with HAGBs in the Al_{2.5}Zn_{2.5}Mg_{2.5}CuYCr and Al_{2.5}Zn_{2.5}Mg_{2.5}CuErCr alloys is 2.5% and 5%, respectively (Figure 9). The fraction of the recrystallized structure with HAGBs of 22.4–25.1% was achieved in the Cr-free Al₃Zn₃Mg₃CuEr(Y) alloys (Figure 9) in the same state. The lower proportion of recrystallized grains results in higher hardness, approximately 110 HV, in the Cr-rich alloys compared to the 85–95 HV observed in the Al₃Zn₃Mg₃CuEr(Y) alloys (Figure 8). This difference is attributed to the formation of E (Al₁₈Mg₃Cr₂) precipitates during the solution treatment.

The increase in hardness in the range of 400–500 °C can be explained by natural aging. The quenching temperature of the alloys is 520 °C. The 1 mm thickness samples were air-cooled after annealing, and the supersaturated solid solution was preserved in the structure. There was an interval of about 5–10 min between air cooling after annealing and hardness measurements. Natural aging hardening in this case was achieved. Increasing the natural aging time to 1 week after annealing at 500 °C provides an increase in hardness to 135 HV and 131 HV in the Al_{2.5}Zn_{2.5}Mg_{2.5}CuYCr and Al_{2.5}Zn_{2.5}Mg_{2.5}CuErCr alloys, respectively. Additionally, the increasing in the annealing temperature to 520 °C at the same time of following natural aging provides a higher hardness of 140 HV and 135 HV due to the formation of a more saturated solid solution.

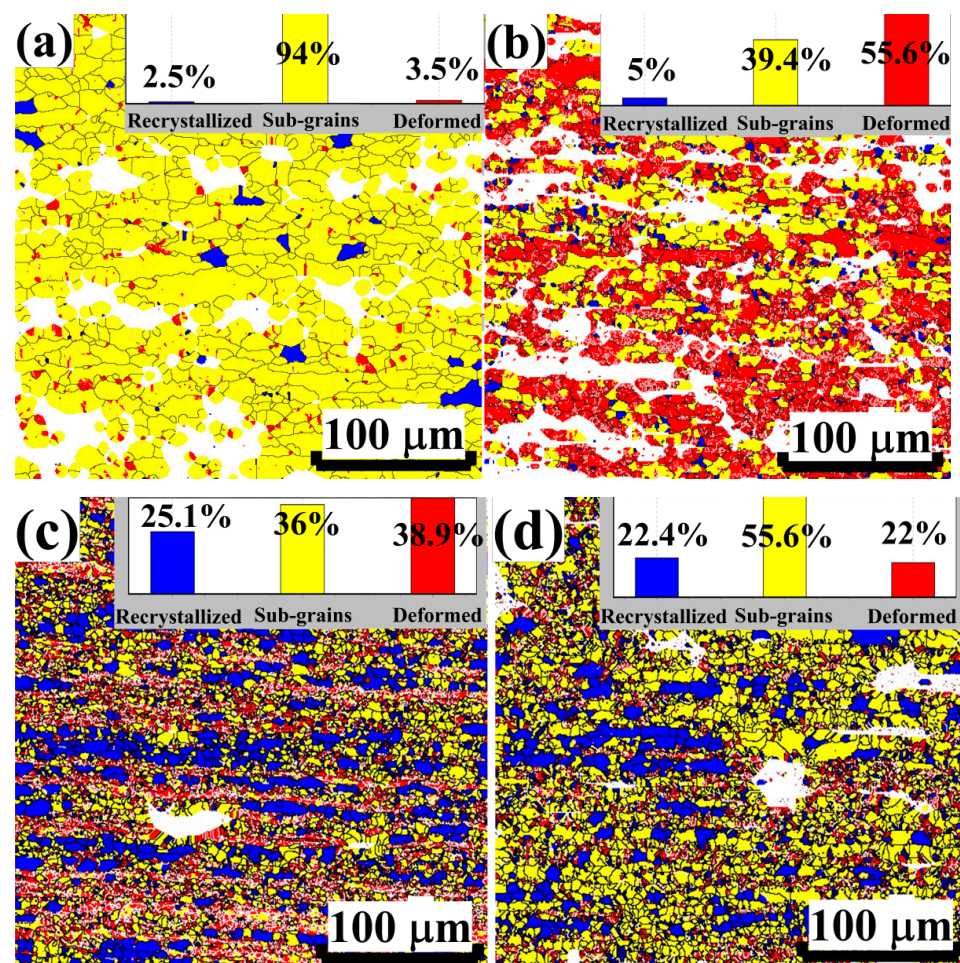


Figure 9. Grain structure of the (a) Al_{12.5}Zn_{2.5}Mg_{2.5}CuYCr, (b) Al_{12.5}Zn_{2.5}Mg_{2.5}CuErCr, (c) Al₃Zn₃Mg₃CuY (adapted from Ref. [21]), and (d) Al₃Zn₃Mg₃CuEr (adapted from Ref. [21]) alloys after 1 h of annealing at 350 °C of rolled sheets (EBSD) (blue—recrystallized grains, yellow—sub-grains, red—deformed grains).

The recrystallization annealing at 520 °C for 15 min and water quenching were applied to the Al_{12.5}Zn_{2.5}Mg_{2.5}CuYCr and Al_{12.5}Zn_{2.5}Mg_{2.5}CuErCr alloys. An average grain size of 10–15 μm is seen in the investigated alloys (Figure 10).

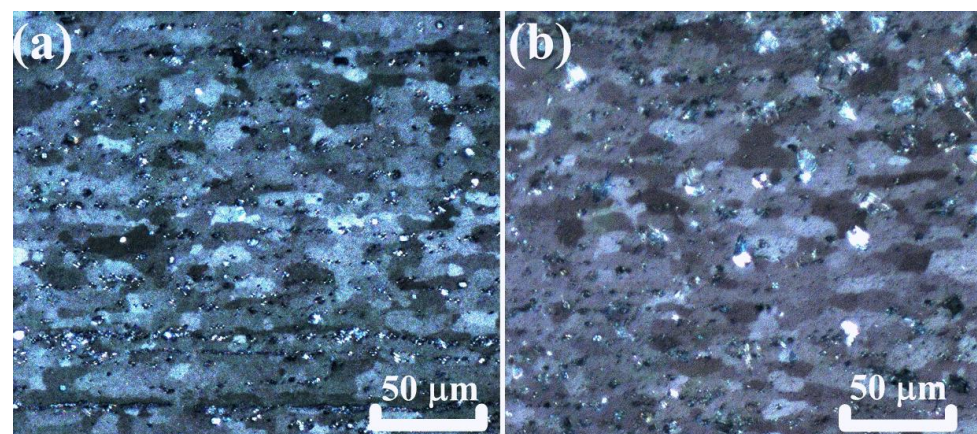


Figure 10. Grain structure of the (a) Al_{12.5}Zn_{2.5}Mg_{2.5}CuYCr and (b) Al_{12.5}Zn_{2.5}Mg_{2.5}CuErCr alloys after 15 min of annealing at 520 °C and water quenching of rolled sheets (polarized light in OM).

3.7. Aging Behavior and Mechanical Properties of Wrought Alloy

The recrystallization annealing at 520 °C for 15 min, water quenching, and natural and artificial aging at 120–210 °C were applied to the Al_{2.5}Zn_{2.5}Mg_{2.5}CuYCr and Al_{2.5}Zn_{2.5}Mg_{2.5}CuErCr alloys sheets. The HV vs time dependencies of the rolled sheet samples at aging temperatures of 120–210 °C (Figure 11) are close to the same aging curves of the cast alloy samples (Figure 6). The YS, UTS, and El. after tensile tests of the aged alloys sheets are collected in Table 9. A good combination of the YS of 280–312 MPa, UTS of 413–470 MPa and elongation (9–17%) was achieved in the Cr doped alloys. The natural aging of the Al_{2.5}Zn_{2.5}Mg_{2.5}CuYCr provides the best combination of strength and plasticity (YS = 300 MPa and El. = 17%). High strength and elongation were achieved after aging at 210 °C, which demonstrates the excellent microstructure stability of the novel alloys (Table 9).

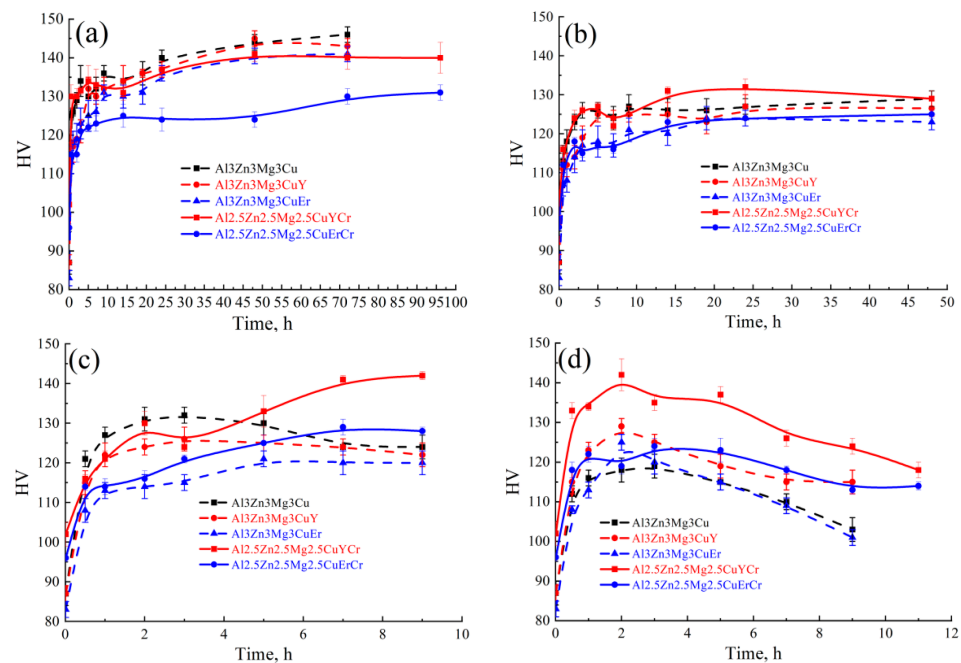


Figure 11. HV vs time dependencies of rolled sheets at aging temperatures of (a) 120 °C, (b) 150 °C, (c) 180 °C, and (d) 210 °C after 15 min of annealing at 520 °C and water quenching.

Table 9. Tensile properties of the rolled, quenched and aged alloys sheets.

State	YS, MPa	UTS, MPa	El., %
Al _{2.5} Zn _{2.5} Mg _{2.5} CuYCr			
As rolled	455 ± 10	476 ± 4	3.2 ± 1.0
520 °C for 15 min/natural aging	300 ± 1	470 ± 10	17 ± 2
520 °C for 15 min/120 °C for 72 h	302 ± 1	437 ± 4	12 ± 2
520 °C for 15 min/150 °C for 24 h	295 ± 1	440 ± 5	16 ± 2
520 °C for 15 min/180 °C for 7 h	280 ± 2	422 ± 3	14 ± 0.2
520 °C for 15 min/210 °C for 2 h	300 ± 3	406 ± 5	9 ± 0.3
Al _{2.5} Zn _{2.5} Mg _{2.5} CuErCr			
As rolled	467 ± 10	490 ± 10	3.4 ± 0.8
520 °C for 15 min/natural aging	280 ± 5	454 ± 4	16 ± 1
520 °C for 15 min/120 °C for 72 h	312 ± 2	446 ± 1	15 ± 0.3
520 °C for 15 min/150 °C for 24 h	292 ± 2	439 ± 4	16.2 ± 0.2
520 °C for 15 min/180 °C for 7 h	293 ± 2	420 ± 3	14 ± 1.0
520 °C for 15 min/210 °C for 2 h	299 ± 3	414 ± 3	12.3 ± 0.5

The novel alloys combine the improved casting properties of the cast Al-Zn-Mg alloys, good strength of the Al-Zn-Mg-Cu alloys, and improved heat resistance of the Al-Cu alloys. The alloys can be classified as cast and wrought aluminum alloys. The cast alloy may be suitable for the aerospace and automobile industry due to good strength at ambient and elevated temperatures and corrosion resistance. The same application is possible as for wrought alloy, due to the good strength and plasticity of the rolled sheets. In addition, good casting properties predict a good weldability.

4. Conclusions

The effects of 0.2%Cr addition on the structure, phase composition, and mechanical properties of the novel cast and wrought Al-2.5Zn-2.5Mg-2.5Cu-0.2Zr-Er(Y) alloys were investigated in detail. Thermodynamic computation (TC) and scanning electron microscopy were used to explain the phase composition of the alloy in the as-cast, solution treated, and aged states.

1. Chromium is distributed between primary crystals (5.7–6.8%) and the aluminum solid solution (0.2%). The primary crystals contain for the main part Al, Cr, Ti, Er(Y) with additional dissolving of Zn, Mg, Cu.

2. The T phase completely dissolved, and the equilibrium phases fragmentized and spheroidized after solution treatment at 520 °C. The experimental phase composition is correlate with TC. The micron sized solidification origin phases ($\text{Al}_8\text{Cu}_4\text{Er}$ (or Y) and Mg_2Si) and supersaturated (Al) with nano sized $\text{Al}_3(\text{Zr,Ti})$ and E ($\text{Al}_{18}\text{Mg}_3\text{Cr}_2$) precipitates are presented in the microstructure of the novel alloys.

3. The nucleation of η (0.5%), S (0.4%), and T (8.8%) precipitates at 180 °C provide the achieving of the maximum hardness of 135 HV in the Al2.5Zn2.5Mg2.5CuYCr alloy. The tensile properties of the novel alloy are slightly lower than those of the referenced alloys, and remain significantly higher than those of the commercial cast 771.0.

4. The corrosion potential of the novel alloy is similar to the E_{cor} of the referenced alloy, but the corrosion current density is still significantly lower due to the formation of E ($\text{Al}_{18}\text{Mg}_3\text{Cr}_2$) precipitates and S phase precipitates of aging origin, in addition to the T phase.

5. The lower proportion of recrystallized grains results in higher hardness in the Cr-rich alloys compared to the referenced alloys due to the formation of E ($\text{Al}_{18}\text{Mg}_3\text{Cr}_2$) precipitates under the solution treatment.

6. High strength and elongation was achieved after aging at 210 °C, which demonstrates the excellent microstructure stability of the novel alloys: $YS = 299\text{--}300$ MPa, $UTS = 406\text{--}414$ MPa, and $El. = 9\text{--}12.3\%$.

The novel alloys combine the improved casting properties of the cast Al-Zn-Mg alloys, a good strength of the Al-Zn-Mg-Cu alloys, and improved heat resistance of the Al-Cu alloys.

Author Contributions: Conceptualization, A.V.P.; methodology, M.V.G. and L.E.G.; formal analysis, M.G.K., A.V.P. and L.E.G.; investigation, M.V.G., R.Y.B., A.V.P. and L.E.G.; data curation, M.V.G., M.G.K., R.Y.B. and L.E.G.; writing—original draft preparation, A.V.P.; writing—review and editing, R.Y.B. and A.V.P.; visualization, A.V.P.; supervision, A.V.P.; funding acquisition, M.G.K. All authors have read and agreed to the published version of the manuscript.

Funding: The work was supported by the Russian Science Foundation (Project No. 22-79-10142), <https://rscf.ru/project/22-79-10142/>.

Data Availability Statement: The raw data supporting the conclusions of this article will be made available by the authors on request.

Conflicts of Interest: The authors declare no conflicts of interest.

References

1. ASM International Handbook Committee. Properties and selection—nonferrous alloys and special-purpose materials. In *ASM Handbook*; ASM International: Metals Park, OH, USA, 2001; Volume 2, ISBN 0871700077.
2. Zolotarevsky, V.S.; Belov, N.A.; Glazoff, M.V. *Casting Aluminum Alloys*; Elsevier: Amsterdam, The Netherlands, 2007; ISBN 9780080453705.
3. Eskin, D.G.; Suyitno; Katgerman, L. Mechanical properties in the semi-solid state and hot tearing of aluminium alloys. *Prog. Mater. Sci.* **2004**, *49*, 629–711. [\[CrossRef\]](#)
4. Pozdniakov, A.V.; Zolotarevskiy, V.S. Determining hot cracking index of Al–Si–Cu–Mg casting alloys calculated using effective solidification range. *Int. J. Cast Met. Res.* **2014**, *27*, 193–198. [\[CrossRef\]](#)
5. Pozdniakov, A.V.; Zolotarevskiy, V.S.; Mamzurina, O.I. Determining hot cracking index of Al–Mg–Zn casting alloys calculated using effective solidification range. *Int. J. Cast Met. Res.* **2015**, *28*, 318–321. [\[CrossRef\]](#)
6. David, M.D.; Foley, R.D.; Griffin, J.A.; Monroe, C.A. Microstructural Characterization and Thermodynamic Simulation of Cast Al–Zn–Mg–Cu Alloys. *Int. J. Met.* **2016**, *10*, 2–20. [\[CrossRef\]](#)
7. Akopyan, T.K.; Belov, N.A.; Alabin, A.N.; Zlobin, G.S. Calculation-experimental study of the aging of casting high-strength Al–Zn–Mg–(Cu)–Ni–Fe aluminum alloys. *Russ. Metall.* **2014**, *2014*, 60–65. [\[CrossRef\]](#)
8. Brodova, I.G.; Shirinkina, I.G.; Rasposienko, D.Y.; Akopyan, T.K. Structural Evolution in the Quenched Al–Zn–Mg–Fe–Ni Alloy during Severe Plastic Deformation and Annealing. *Phys. Met. Metallogr.* **2020**, *121*, 899–905. [\[CrossRef\]](#)
9. Raabe, D.; Tasan, C.C.; Olivetti, E.A. Strategies for improving the sustainability of structural metals. *Nature* **2019**, *575*, 64–74. [\[CrossRef\]](#) [\[PubMed\]](#)
10. Stemper, L.; Tunes, M.A.; Tosone, R.; Uggowitzer, P.J.; Pogatscher, S. On the potential of aluminum crossover alloys. *Prog. Mater. Sci.* **2022**, *124*, 100873. [\[CrossRef\]](#)
11. Zhang, Z.; Li, Y.; Li, H.; Zhang, D.; Zhang, J. Effect of high Cu concentration on the mechanical property and precipitation behavior of Al–Mg–Zn–(Cu) crossover alloys. *J. Mater. Res. Technol.* **2022**, *20*, 4585–4596. [\[CrossRef\]](#)
12. Zhang, L.; Peng, G.; Gu, Y.; Chen, S.; Li, J. Composition optimization and mechanical properties of Al–Zn–Mg–Si–Mn crossover alloys by orthogonal design. *Mater. Chem. Phys.* **2023**, *307*, 128216. [\[CrossRef\]](#)
13. Zhang, Z.; Li, Y.; Liu, Y.; Li, H.; Zhang, D.; Zhang, J. A novel Al–Mg–Zn–(Cu) crossover alloy with ultra-high strength. *Mater. Lett.* **2023**, *347*, 134640. [\[CrossRef\]](#)
14. Zhang, X.; Yang, C.; Meng, L.; Chen, Z.; Gong, W.; Sun, B.; Zhao, S.; Zhang, D.; Li, Y.; Zhou, D. The influence of precipitation on plastic deformation in a high Mg-containing AlMgZn-based crossover alloy: Slip localization and strain hardening. *Int. J. Plast.* **2024**, *173*, 103896. [\[CrossRef\]](#)
15. Trink, B.; Weißensteiner, I.; Uggowitzer, P.J.; Strobel, K.; Hofer-Roblyek, A.; Pogatscher, S. Processing and microstructure–property relations of Al–Mg–Si–Fe crossover alloys. *Acta Mater.* **2023**, *257*, 119160. [\[CrossRef\]](#)
16. Zhang, Z.; Hao, Z.; Wang, H.; Zhang, D.; Zhang, J. Modifying the microstructure and stress distribution of crossover Al–Mg–Zn alloy for regulating stress corrosion cracking via retrogression and re-aging treatment. *Mater. Sci. Eng. A* **2023**, *884*, 145564. [\[CrossRef\]](#)
17. Tan, P.; Liu, Z.; Qin, J.; Wei, Q.; Wang, B.; Yi, D. Enhanced corrosion performance by controlling grain boundary precipitates in a novel crossover Al–Cu–Zn–Mg alloy by optimizing Zn content. *Mater. Charact.* **2024**, *208*, 113615. [\[CrossRef\]](#)
18. Gerchikova, N.S.; Fridlyander, I.N.; Zaitseva, N.I.; Kirkina, N.N. Change in the structure and properties of Al–Zn–Mg alloys. *Met. Sci. Heat Treat.* **1972**, *14*, 233–236. [\[CrossRef\]](#)
19. Zou, Y.; Wu, X.; Tang, S.; Zhu, Q.; Song, H.; Guo, M.; Cao, L. Investigation on microstructure and mechanical properties of Al–Zn–Mg–Cu alloys with various Zn/Mg ratios. *J. Mater. Sci. Technol.* **2021**, *85*, 106–117. [\[CrossRef\]](#)
20. Pan, Y.; Zhang, D.; Liu, H.; Zhuang, L.; Zhang, J. Precipitation hardening and intergranular corrosion behavior of novel Al–Mg–Zn–(Cu) alloys. *J. Alloys Compd.* **2021**, *853*, 157199. [\[CrossRef\]](#)
21. Glavatskikh, M.V.; Barkov, R.Y.; Gorlov, L.E.; Khomutov, M.G.; Pozdniakov, A.V. Novel Cast and Wrought Al–3Zn–3Mg–3Cu–Zr–Y(Er) Alloys with Improved Heat Resistance. *Metals* **2023**, *13*, 909. [\[CrossRef\]](#)
22. Amer, S.M.; Barkov, R.Y.; Prosviryakov, A.S.; Pozdniakov, A.V. Structure and Properties of New Heat-Resistant Cast Alloys Based on the Al–Cu–Y and Al–Cu–Er Systems. *Phys. Met. Metallogr.* **2021**, *122*, 908–914. [\[CrossRef\]](#)
23. Gao, H.; Feng, W.; Wang, Y.; Gu, J.; Zhang, Y.; Wang, J.; Sun, B. Structural and compositional evolution of Al₃(Zr,Y) precipitates in Al–Zr–Y alloy. *Mater. Charact.* **2016**, *121*, 195–198. [\[CrossRef\]](#)
24. Wen, S.P.; Gao, K.Y.; Li, Y.; Huang, H.; Nie, Z.R. Synergetic effect of Er and Zr on the precipitation hardening of Al–Er–Zr alloy. *Scr. Mater.* **2011**, *65*, 592–595. [\[CrossRef\]](#)
25. Li, H.; Bin, J.; Liu, J.; Gao, Z.; Lu, X. Precipitation evolution and coarsening resistance at 400 °C of Al microalloyed with Zr and Er. *Scr. Mater.* **2012**, *67*, 73–76. [\[CrossRef\]](#)
26. Wen, S.P.; Gao, K.Y.; Huang, H.; Wang, W.; Nie, Z.R. Precipitation evolution in Al–Er–Zr alloys during aging at elevated temperature. *J. Alloys Compd.* **2013**, *574*, 92–97. [\[CrossRef\]](#)
27. Gao, Z.; Li, H.; Lai, Y.; Ou, Y.; Li, D. Effects of minor Zr and Er on microstructure and mechanical properties of pure aluminum. *Mater. Sci. Eng. A* **2013**, *580*, 92–98. [\[CrossRef\]](#)
28. Li, H.; Gao, Z.; Yin, H.; Jiang, H.; Su, X.; Bin, J. Effects of Er and Zr additions on precipitation and recrystallization of pure aluminum. *Scr. Mater.* **2013**, *68*, 59–62. [\[CrossRef\]](#)

29. Huang, H.; Wen, S.P.; Gao, K.Y.; Wang, W.; Nie, Z.R. Age hardening behavior and corresponding microstructure of dilute Al-Er-Zr alloys. *Metall. Mater. Trans. A Phys. Metall. Mater. Sci.* **2013**, *44*, 2849–2856. [\[CrossRef\]](#)
30. Nokhrin, A.V.; Nagicheva, G.S.; Chuvil'deev, V.N.; Kopylov, V.I.; Bobrov, A.A.; Tabachkova, N.Y. Effect of Er, Si, Hf and Nb Additives on the Thermal Stability of Microstructure, Electrical Resistivity and Microhardness of Fine-Grained Aluminum Alloys of Al-0.25%Zr. *Materials* **2023**, *16*, 2114. [\[CrossRef\]](#)
31. Wen, L.; Liu, W.; Wu, G.; Wu, H.; Zhang, L.; Sun, J.; Zhang, J.; Xu, S.; Shi, C.; Wang, Y.; et al. Microstructure and stress corrosion cracking resistance of Al-6.5Zn-2Cu-1.5Mg-0.05Ti alloy modified by Cr addition. *Mater. Charact.* **2022**, *183*, 111621. [\[CrossRef\]](#)
32. Ding, L.; Zhao, L.; Weng, Y.; Schryvers, D.; Liu, Q.; Idrissi, H. Atomic-scale investigation of the heterogeneous precipitation in the E (Al₁₈Mg₃Cr₂) dispersoid of 7075 aluminum alloy. *J. Alloys Compd.* **2021**, *851*, 156890. [\[CrossRef\]](#)
33. Fang, H.C.; Chen, K.H.; Chen, X.; Chao, H.; Peng, G.S. Effect of Cr, Yb and Zr additions on localized corrosion of Al-Zn-Mg-Cu alloy. *Corros. Sci.* **2009**, *51*, 2872–2877. [\[CrossRef\]](#)
34. Fang, H.C.; Chao, H.; Chen, K.H. Effect of Zr, Er and Cr additions on microstructures and properties of Al-Zn-Mg-Cu alloys. *Mater. Sci. Eng. A* **2014**, *610*, 10–16. [\[CrossRef\]](#)
35. Wang, M.; Huang, L.; Chen, K.; Liu, W. Influence of minor combined addition of Cr and Pr on microstructure, mechanical properties and corrosion behaviors of an ultrahigh strength Al-Zn-Mg-Cu-Zr alloy. *Micron* **2018**, *104*, 80–88. [\[CrossRef\]](#) [\[PubMed\]](#)
36. Chen, K.H.; Fang, H.C.; Zhang, Z.; Chen, X.; Liu, G. Effect of Yb, Cr and Zr additions on recrystallization and corrosion resistance of Al-Zn-Mg-Cu alloys. *Mater. Sci. Eng. A* **2008**, *497*, 426–431. [\[CrossRef\]](#)
37. Wang, Y.; Cao, L.; Wu, X.; Lin, X.; Yao, T.; Peng, L. Multi-alloying effect of Ti, Mn, Cr, Zr, Er on the cast Al-Zn-Mg-Cu alloys. *Mater. Charact.* **2023**, *201*, 112984. [\[CrossRef\]](#)
38. Lin, G.; Zheng, X.; Yang, W.; Feng, D.; Peng, D. Study on the hot deformation behavior of Al-Zn-Mg-Cu-Cr aluminum alloy during multi-stage hot compression. *Acta Metall. Sin. (Engl. Lett.)* **2009**, *22*, 110–116. [\[CrossRef\]](#)
39. Fang, H.C.; Chen, K.H.; Chen, X.; Huang, L.P.; Peng, G.S.; Huang, B.Y. Effect of Zr, Cr and Pr additions on microstructures and properties of ultra-high strength Al-Zn-Mg-Cu alloys. *Mater. Sci. Eng. A* **2011**, *528*, 7606–7615. [\[CrossRef\]](#)
40. Peng, G.; Chen, K.; Fang, H.; Chen, S. Effect of Cr and Yb additions on microstructure and properties of low copper Al-Zn-Mg-Cu-Zr alloy. *Mater. Des. (1980–2015)* **2012**, *36*, 279–283. [\[CrossRef\]](#)
41. Fang, H.C.; Luo, F.H.; Chen, K.H. Effect of intermetallic phases and recrystallization on the corrosion and fracture behavior of an Al-Zn-Mg-Cu-Zr-Yb-Cr alloy. *Mater. Sci. Eng. A* **2017**, *684*, 480–490. [\[CrossRef\]](#)
42. Lin, G.Y.; Zhang, Z.F.; Zhang, H.; Peng, D.S.; Zhou, J. Study on the hot deformation behaviors of Al-Zn-Mg-Cu-Cr aluminum alloy. *Acta Metall. Sin. (Engl. Lett.)* **2008**, *21*, 109–115. [\[CrossRef\]](#)
43. He, Y.; Zhang, X.; Cao, Z. Effect of Minor Cr, Mn, Zr, Ti and B on Grain Refinement of As-Cast Al-Zn-Mg-Cu Alloys. *Rare Met. Mater. Eng.* **2010**, *39*, 1135–1140. [\[CrossRef\]](#)
44. An, Z.; Yang, W.; Zhan, H.; Hu, B.; Wang, Q.; Matsumura, S.; Sha, G. On the strengthening effect of Al-Cr-Si dispersoid in an Al-Si-Mg-Cu casting alloy with Cr addition. *Mater. Charact.* **2020**, *166*, 110457. [\[CrossRef\]](#)
45. Arriaga-Benitez, R.I.; Pekguleryuz, M. The synergistic effects of nano-sized α -Al(Mn,Cr,Fe)Si and Al-Si-Zr dispersoids on the creep behavior Al-Si-Mg-Cu (Mn, Cr, Zr) diesel engine alloy. *Mater. Sci. Eng. A* **2023**, *872*, 144949. [\[CrossRef\]](#)
46. Fang, H.C.; Shang, P.J.; Huang, L.P.; Chen, K.H.; Liu, G.; Xiong, X. Precipitates and precipitation behavior in Al-Zr-Yb-Cr alloys. *Mater. Lett.* **2012**, *75*, 192–195. [\[CrossRef\]](#)
47. Amer, S.M.; Glavatskikh, M.V.; Barkov, R.Y.; Loginova, I.S.; Pozdniakov, A.V. Effect of chromium on microstructure and mechanical properties of the Al-Cu-Er-Zr alloy. *Metallurgist* **2024**, *in press*. [\[CrossRef\]](#)
48. Amer, S.M.; Glavatskikh, M.V.; Barkov, R.Y.; Loginova, I.S.; Pozdniakov, A.V. Effect of Mn substitution on Cr in the Al-Cu-Er-Mg-Zr-Fe-Si-Ti cast alloy. *J. Alloys Compd.* **2024**, *983*, 173958. [\[CrossRef\]](#)
49. Liu, X.; Wang, B.; Li, Q.; Wang, J.; Zhang, C.; Xue, C.; Yang, X.; Tian, G.; Liu, X.; Tang, H. Quantifying the Effects of Grain Refiners Al-Ti-B and La on the Microstructure and Mechanical Properties of W319 Alloy. *Metals* **2022**, *12*, 627. [\[CrossRef\]](#)
50. Wei, C.; Zhan, Y. Phase-Equilibrium Investigation of the Al-Cr-Er Ternary System at 773 K (500 °C). *Metall. Mater. Trans. A* **2019**, *50*, 2956–2970. [\[CrossRef\]](#)
51. Raghavan, V. Al-Cr-Cu (Aluminum-Chromium-Copper). *J. Phase Equilibria Diffus.* **2012**, *33*, 53–54. [\[CrossRef\]](#)
52. Raghavan, V. Al-Er-Mg (Aluminum-Erbium-Magnesium). *J. Phase Equilibria Diffus.* **2007**, *28*, 461–463. [\[CrossRef\]](#)
53. Rogl, P.; Stiltz, S.; Hayes, F.H. The Al-Cr-Mg system aluminum-chromium-magnesium. *JPE* **1992**, *13*, 317–323. [\[CrossRef\]](#)
54. Xu, L.; Lv, J.; Tang, H.; Huang, D. Phase equilibria and solidification characteristics in the Al-rich region of the Al-Ti-Er system. *J. Alloys Compd.* **2024**, *980*, 173667. [\[CrossRef\]](#)
55. Kishchik, M.S.; Mochugovskiy, A.G.; Cuda, M.; Kishchik, A.A.; Mikhaylovskaya, A.V. Particle Stimulated Nucleation Effect for Al-Mg-Zr-Sc Alloys with Ni Addition during Multidirectional Forging. *Metals* **2023**, *13*, 1499. [\[CrossRef\]](#)
56. Mosleh, A.O.; Yakovtseva, O.A.; Kishchik, A.A.; Kotov, A.D.; Moustafa, E.B.; Mikhaylovskaya, A.V. Effect of Coarse Eutectic-Originated Particles on the Microstructure and Properties of the Friction Stir-Processed Al-Mg-Zr-Sc-Based Alloys. *JOM* **2023**, *75*, 2989–3000. [\[CrossRef\]](#)
57. Kishchik, A.A.; Mikhaylovskaya, A.V.; Kotov, A.D.; Rofman, O.V.; Portnoy, V.K. Al-Mg-Fe-Ni based alloy for high strain rate superplastic forming. *Mater. Sci. Eng. A* **2018**, *718*, 190–197. [\[CrossRef\]](#)

58. Amer, S.M.; Mikhaylovskaya, A.V.; Barkov, R.Y.; Kotov, A.D.; Mochugovskiy, A.G.; Yakovtseva, O.A.; Glavatskikh, M.V.; Loginova, I.S.; Medvedeva, S.V.; Pozdniakov, A.V. Effect of Homogenization Treatment Regime on Microstructure, Recrystallization Behavior, Mechanical Properties, and Superplasticity of Al-Cu-Er-Zr Alloy. *JOM* **2021**, *73*, 3092–3101. [[CrossRef](#)]
59. Mikhaylovskaya, A.V.; Kotov, A.D.; Barkov, R.Y.; Yakovtseva, O.A.; Glavatskikh, M.V.; Loginova, I.S.; Pozdniakov, A.V. The Influence of Y and Er on the Grain Structure and Superplasticity of Al-Cu-Mg-Based Alloys. *JOM* **2024**, *76*, 1821–1830. [[CrossRef](#)]
60. Mochugovskiy, A.G.; Prosviryakov, A.S.; Tabachkova, N.Y.; Mikhaylovskaya, A.V. The Effect of Ce on the Microstructure, Superplasticity, and Mechanical Properties of Al-Mg-Si-Cu Alloy. *Metals* **2022**, *12*, 512. [[CrossRef](#)]

Disclaimer/Publisher’s Note: The statements, opinions and data contained in all publications are solely those of the individual author(s) and contributor(s) and not of MDPI and/or the editor(s). MDPI and/or the editor(s) disclaim responsibility for any injury to people or property resulting from any ideas, methods, instructions or products referred to in the content.